Biochemical Pharmacology 90 (2014) 145–158

Contents lists available at ScienceDirect

Biochemical Pharmacology

journal homepage: www.elsevier.com/locate/biochempharm

Structural and energetic analysis to provide insight residues of CYP2C9, 2C11 and 2E1 involved in valproic acid dehydrogenation selectivity

Martiniano Bello *, Jessica E. Mendieta-Wejebe, José Correa-Basurto *

Laboratorio de Modelado Molecular, Bioinformática y Diseño de Fármacos de la Escuela Superior de Medicina, Instituto Politécnico Nacional, Plan de San Luis y Díaz Mirón s/n, Casco de Santo Tomás, México, Distrito Federal 11340, Mexico

ARTICLE INFO

Article history:
Received 13 March 2014
Accepted 25 April 2014
Available online 2 May 2014

Keywords:
Drug metabolism
CYP450 enzymes
Molecular dynamics simulations
Molecular mechanics generalized born surface area

ABSTRACT

Docking and molecular dynamics (MD) simulation have been two computational techniques used to gain insight about the substrate orientation within protein active sites, allowing to identify potential residues involved in the binding and catalytic mechanisms. In this study, both methods were combined to predict the regioselectivity in the binding mode of valproic acid (VPA) on three cytochrome P-450 (CYP) isoforms CYP2C9, CYP2C11, and CYP2E1, which are involved in the biotransformation of VPA yielding reactive hepatotoxic intermediate 2-*n*-propyl-4-pentenoic acid (4*n*VPA). There are experimental data about hydrogen atom abstraction of the C4-position of VPA to yield 4*n*VPA, however, there are not structural evidence about the binding mode of VPA and 4*n*VPA on CYPs. Therefore, the complexes between these CYP isoforms and VPA or 4*n*VPA were studied to explore their differences in binding and energetic stabilization. Docking results showed that VPA and 4*n*VPA are coupled into CYPs binding site in a similar conformation, but it does not explain the VPA hydrogen atom abstraction. On the other hand, MD simulations showed a set of energetic states that reorient VPA at the first ns, then making it susceptible to a dehydrogenation reaction. For 4*n*VPA, multiple binding modes were observed in which the different states could favor either undergo other reaction mechanism or ligand expulsion from the binding site. Otherwise, the energetic and entropic contribution point out a similar behavior for the three CYP complexes, showing as expected a more energetically favorable binding free energy for the complexes between CYPs and VPA than with 4*n*VPA.

1. Introduction

Valproic acid (VPA, Fig. 1) is an important antiepileptic drug that has been widely used in the management of various types of seizure disorders [1]. Although VPA is considered a relatively safe drug, in some occasions, it may associate with severe and sometimes fatal liver injury [2]. Although the mechanism of VPA hepatotoxicity is not understood so far, there are multiple factors that could contribute to the toxicity, including (1) formation of reactive metabolites of VPA [3] and the subsequent covalent binding to cellular proteins [4–6], and (2) development of oxidative stress [7].

In the course of the characterization of the metabolism of VPA, it was discovered that there were multiple metabolic pathways involved in its biotransformation which give rise to more than 50 known metabolites of the parent drug [8]. However, from these multiple pathways, the oxidative metabolism of VPA by cytochrome P450 (CYP) constitutes a minor metabolic pathway, but it represents the one which generates the hepatotoxic metabolite 2-*n*-propyl-4-pentenoic acid (4*n*VPA) in liver microsomes from rats, mice, rabbits and humans [9]. Experiments using deuterated analogs of VPA to obtain evidence about the dehydrogenation reaction demonstrated that this reaction proceeds via hydrogen atom abstraction of the C4-position [9]. The metabolism of VPA to 4*n*VPA represents a dehydrogenation reaction of a sp^3 hybridized center, which is not adjacent to any sp^2 hybridized carbon center. The metabolite arises by either abstraction of a second hydrogen atom by the Fe(IV)–OH intermediate and subsequent collapse of the diradical or via abstraction of an electron and deprotonation

Abbreviations: CYP, cytochrome P-450; CYP2C9, cytochrome P-450 C9; CYP2C11, cytochrome P-450 C11; CYP2E1, cytochrome P-450 E1; MD, molecular dynamics; MM-GBSA, molecular mechanics generalized born surface area; PDB, protein data bank; RMSD, root mean square deviation; 3D, three-dimensional; VPA, valproic Acid; 4*n*VPA, 2-*n*-propyl-4-pentenoic acid; VMD, visual molecular dynamics.

* Corresponding authors.
E-mail addresses: mbellor@ipn.mx, bellomartini@gmail.com (M. Bello), jcorrea-b@ipn.mx, corrjose@gmail.com (J. Correa-Basurto).

http://dx.doi.org/10.1016/j.bcp.2014.04.016

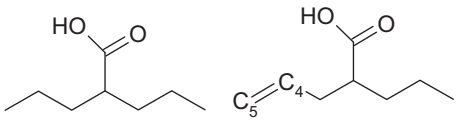

Fig. 1. Chemical structures of VPA (left) and 4*n*VPA (right).

of the cationic intermediate to yield the alkene [10,11]. However, although this kind of biochemical reaction is unusual in nature; there are several cases where this reaction has been observed [10–16].

CYP is a superfamily of cysteinato-heme enzymes [10,17]. Its active site contains a heme, which is deeply buried inside the protein at the bottom of a large, internal binding cavity. Heme unit consists of an iron protoporphyrin IX complex with a cysteine (Cys) residue as the proximal axial ligand. The active catalytic species, with a Fe(IV)-oxo moiety, is commonly denoted as Compound I. These enzymes are potent oxidants involved in oxidizing reactions such as the hydroxylation of saturated carbon-hydrogen bonds, the epoxidation of double bonds, the oxidation of heteroatoms, dealkylation reactions, and oxidations of aromatics using dioxygen to catalyze a great variety of stereospecific and regioselective processes of oxygen insertion into a variety of organic compounds, both of endogenous (such as steroids) and exogenous (xenobiotics) origins [18–23]. Furthermore, CYP enzymes can also catalyze the dehydrogenation of some organic molecules instead of carrying out the oxygenation of the substrate as observed for VPA and other organic molecules [24]. In this manner, CYP converts all the dioxygen into water and generates an olefin, thus exhibiting a mixed function as an oxidase-dehydrogenase enzyme.

The CYP enzymes share common structural characteristics such as a common overall fold despite less than 20% sequence identity across the CYP gene superfamily [23]. In recent years, the elucidation of several complexes of CYP crystal structures has provided further insight into the important structural aspects of these critical interactions, pointing out that steric and electronic parameters of the enzyme active site residues facilitate dehydratation or dehydrogenation reactions by positioning the substrate and/or stabilizing transition states [25,26]. On the other hand, although we have a general understanding about how 4*n*VPA is formed [9], the precise mechanisms or factors that direct dehydrogenation versus oxygenation are not well understood. Because human CYP2C9, CYP2E1 and rat CYP2C11 have been reported as VPA metabolizing in liver microsomes and also involved in 4*n*VPA formation [27], elucidating the factors that control its dehydrogenation is crucial to the design of analog drugs with reduced risks of metabolic activation.

Molecular models are valuable tools for studying substrate orientation within the CYP active site [28–31]. Nevertheless, the predictive power of these procedures is highly dependent on several factors, such as the accurate of the three-dimensional (3D) structure used as target [32,33] and the force field parameters for accurately determining the interactions between a compound and its target [34]. Bioinformatics methods have been widely used to predict ligand conformation into CYPs binding sites [13,35]. Moore et al. performed docking studies to model the metabolism of raloxifene, a CYP3A4-mediated dehydrogenated substrate [13]. Molecular docking is a method that predicts the binding mode of a ligand to a protein, and has been extensively used in rational design of drug [36–38]. However, some researcher have mentioned that the conformations obtained through docking procedures need to be examined by molecular dynamic (MD) simulations [39,40]. Therefore, in order to propose a plausible binding conformation between VPA or 4*n*VPA and CYPs that would allow to explain the binding orientation of both ligands into CYPs binding site as to be susceptible to undergo a dehydrogenation reaction, we carried out automatic molecular docking using AutoDock software. Afterward, the dynamic stability of these complexes conformations were further analyzed using MD simulations, together with binding free energy estimation using the Molecular Mechanics Generalized Born Surface Area (MMGBSA) method.

To develop this study, we utilized two X-ray crystal structures of human beings (CYP2C9 and CYP2E1) and a model from rat (CYP2C11), which was obtained through homology modeling procedures. Structural analysis shows that CYP2C9, CYP2C11, and CYP2E1 share a similar overall folding structure (Fig. 2A), where the substrate binding cavity is formed by similar secondary structure elements: helices I, F, G, and F–G, B–C loops (Fig. 2B). These CYPs structures were chosen because it has been reported that both human enzymes catalyze the dehydrogenation of VPA [41–43], whereas that CYP2C11 is one of the most active and versatile CYP in rat liver microsomes [44–47] and the one used widely in our laboratory to evaluate the VPA metabolism. Thus, in overall our aim in this study is to determine whether or not the dehydrogenation mechanism was consistent among CYP enzymes or differences were possible among the isoforms. Finally, our results demonstrate the utility of these combined techniques in evaluating the intricate interactions between dehydrogenated substrates and CYP enzymes.

2. Methods

2.1. Homology modeling of CYP2C11

Since the crystal structure of CYP2C11 is not available so far in the Protein Data Bank (PDB), the 3D model of CYP2C11 used in the present contribution was constructed based on a homology modeling method using the known 3D structures of CYP2C9 (1R9O) and CYP2E1 (3KOH) as templates, and under the following procedure. First, we explored the NCBI protein data base [http://www.ncbi.nlm.nih.gov/sites/entrez] to search the amino acid sequences of rat CYP2C11 (Swiss-prot entry code: P08683). The ClustalW program version 2.0 [48] was used to identify similarity of this sequence to other CYP structures, and the I-TASSER server [49] was used to generate the 3D model. Once obtained the latter, this was minimized using MD simulations and its dihedral angles were validated by checking its Ramachandran map. Afterward, a protein sequence alignment among the CYP2C11 sequence, and those of templates (CY2C9 (1R9O) and CYP2E1 (3KOH)) was performed using ClustalW program [48] to evaluate the percentage of identity among the three CYP sequences, whereas that the level of conservation for each residue was calculated using PRALINE server [50].

2.2. Automated docking

AutoDock version 4.0.1 [51] was used to perform the automated docking studies between VPA or 4*n*VPA versus CYPs. Both substrates were treated as flexible ligands by modifying their rotatable torsions, but CYP2C9 (Fig. 2C), CYP2C11 and CYP2E1 (Fig. 2D and E) template were considered to be a rigid protein. 3D coordinates of the CYP2C9 and CYP2E1 structures 1R9O and 3KOH, respectively, were acquired from the PDB, whereas CYP2C11 was constructed using homology modeling procedures (see Section 2.1). X-ray structures were cleaned of both water molecules and co-crystallized ligands.

The substrate structures were drawn using the Isis/Draw program [52], and then were converted to a 3D format using WebLab Viewer and Molekel Visualization Package [53,54]. A geometric pre-optimization was carried out by using HyperChem 6.0 [55]. The minimum energy structure of the ligands was obtained using a semi-empical method at the AM1 level by

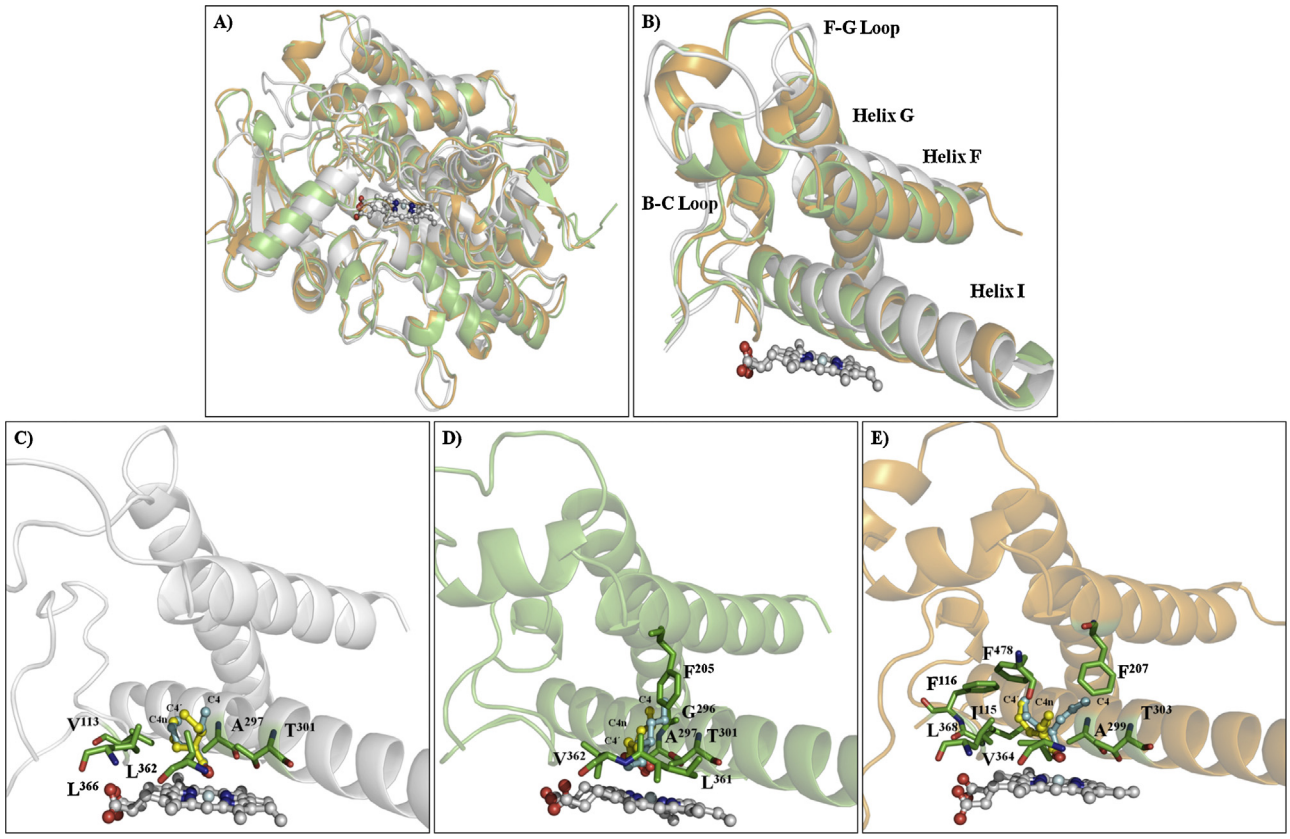

Fig. 2. Superposition of the overall folding and molecular models of VPA and 4*n*VPA in the substrate binding site of CYP2C9, CYP2C11, and CYP2E1 predicted by AutoDock version 4.0.1. Folding structures (A) and substrate binding sites (B) of CYP2C9 (white), 2C11 (green), and 2E1 (orange), structures are shown in cartoon representations, and the heme group is represented with white spheres. The RMSD values between CYP2C9 and CYP2C11 or CYP2E1 were 1.692 or 1.578, respectively. VPA or 4*n*VPA was docked into CYPs, and a representative conformation from the largest and lowest-energy cluster, predicted dehydrogenation from docking between VPA (cyan stick representation) or 4*n*VPA (yellow stick representation) and CYP2C9 (C); that from docking with CYP2C11 is shown in panel (D), and that from docking with CYP2E1 is depicted in panel (E).

Gaussian 03 [56]. The partial atomic charges (Gasteiger–Marsili formalism) and all rotatable bonds of the ligands as well as the Kollmand charges for all the protein atoms were assigned by AutoDock Tools [51].

To define the binding sites in which the substrates moved, AutoGrid version 3.06 [51] was used. First, rectangular grid boxes were constructed over all proteins (47.798, 34.060 and 54.683 $Å^3$, for CYP2C9), (57.950, 57.040 and 57.940 $Å^3$, for CYP2C11) and (65.660, 67.520 and 62.560 $Å^3$, for CYP2E1) with the grid points separated by 0.375 Å, centered on the ligand binding pocket (upper iron atom at 1.9 Å). The box size was decreased to force the ligands to enter at the active site.

All docking simulations were carried out by using the hybrid Lamarckian Genetic Algorithm, with an initial population of 100 randomly placed individuals and a maximum number of 1.0×10^7 energy evaluations. The resulting docked orientations within a root-mean square deviation (RMSD) of 0.5 Å were clustered together. The lowest energy cluster returned by AutoDock for each compound was used for further analysis. All other parameters were maintained at their default settings.

Finally, to determine whether a ligand could be recognized by the proteins, one ligand was first docked following the conditions mentioned earlier, using the box size $120 \times 120 \times 120$ $Å^3$. Then, its coordinates were pasted to proteins PDB structures, obtaining a protein-ligand complex.

2.3. Molecular dynamics (MD) simulations

A series of MD simulations were carried out for all complexes obtained under docking procedures (see Section 2.2). The simulations and the analysis of the trajectories were performed with Amber 12 package [57] using the FF99SB force field [58]. Complexes were constructed using the Leap module, minimized by the sander module, and the "pmemd" module was used for MD simulations. The ligand parameters were estimated with the antechamber module, based on the general AMBER force field (GAFF) [59], followed by ab initio optimization of ligands at the AM1-BCC level [60]. The missing force field parameters for Heme (all-atom) group were taken from the AMBER parameter database [61]. Cl^- ions were placed by Leap to neutralize the positive charges of areas around the complex models at pH 7. A rectangular-shaped box of water was constructed using the TIP3P water model [62], with a margin of 12.0 Å in each direction from the solute. The systems were then equilibrated by a 500 ps of energy minimization with position restraints on the protein and ligand to allow for relaxation of the solvent molecules. The equilibration run was followed by a 50 ns MD run without position restraints under periodic boundary conditions.

The non-bonded list was generated using an atom-based cutoff of 8.0 Å. The electrostatic term was described with the particle mesh Ewald algorithm [63]. The time step of the MD simulations was set to 2.0 fs, and the SHAKE algorithm [64] was used to constrain bond lengths at their equilibrium values. Temperature and pressure were maintained using the weak-coupling algorithm [65] with coupling constants τ_T and τ_P of 1.0 and 0.2 ps, respectively (300 K, 1 atm). Coordinates were saved for analyses every 1 ps. Analysis of the trajectories was performed using AMBER analysis tools [57] and PyMOL [66].

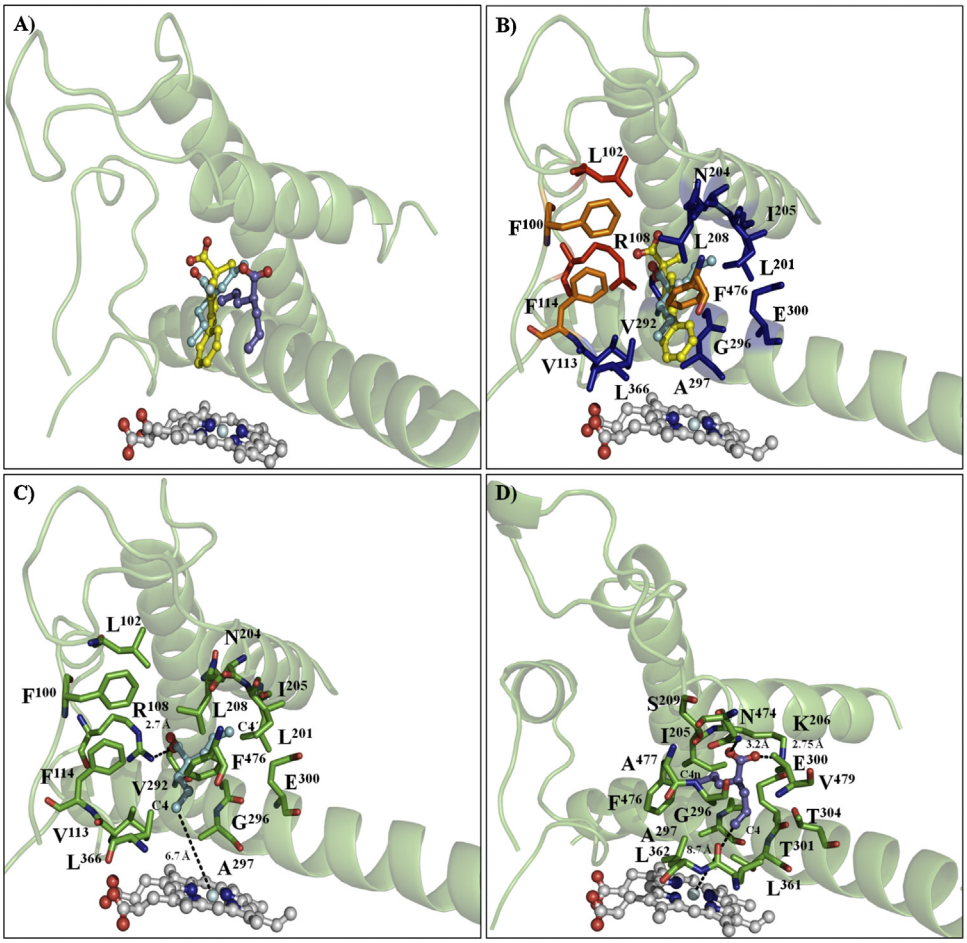

Fig. 3. Average conformations of CYP2C9–VPA, CYP2C9–4*n*VPA complex and the crystallographic structure of the CYP2C9–FLP complex. (A) Structural superposition of the average conformations of CYP2C9–VPA, CYP2C9–4*n*VPA, and CYP2C9–FLP complex. (B) Residues constituting the hydrophobic cleft (V^{113}, L^{201}, N^{204}, I^{205}, L^{208}, V^{292}, G^{296}, A^{297}, E^{300}, and L^{366}), narrow solvent channel (L^{102} and R^{108}), and the Phe cluster (F^{100}, F^{114} and F^{476}), are rendered as blue, orange and red stick representations, respectively. Residues stabilizing the VPA (C) or 4*n*VPA (D) conformation within 4 Å are depicted in green stick representation. VPA, 4*n*VPA, and FLP are shown in cyan, yellow, and blue ball and stick representations, respectively. Oxygen, nitrogen, and FE are colored red, blue, and cyan. For reference, the heme is shown as ball and stick figure colored white, and structural elements building the folding and substrate binding cavity are rendered as cartoon figures. The average conformations were calculated over the final 40-ns of the MD simulations.

2.3.1. Calculation of binding free energy

Binding free energies were calculated using MM-GBSA approach supplied with Amber 12 package [57], using a salt concentration of 0.1 M, and the Born implicit solvent model of 2 (igb = 2) [67]. For the CYP2C9–VPA (Fig. 3C) and CYP2C9–4*n*VPA (Fig. 3D) complexes, the binding free energy was calculated using 400 snapshots of each model at time intervals of 100 ps from the last 40-ns production runs. For the four CYP2C11–VPA conformations present during the last 40-ns of MD simulations, the binding free energies were calculated using 150 snapshots for CYP2C11–VPA_c (Fig. 4C, 10–25 ns), 50 snapshots CYP2C11–VPA_{d-e} (Fig. 4D and E, 25–30 ns), and 200 snapshots CYP2C11–VPA_f (Fig. 4F, 30–50 ns). From the two CYP2C11–4*n*VPA conformations present during the last 40-ns of MD simulations, the binding free energy for the most representative conformation was calculated using 350 snapshots (Fig. 4G, 10–45 ns). From the three CYP2E1–VPA (depicting a superposition of VPA and 4*n*VPA, Fig. 5A and B) conformations present during de MD simulation, the binding free energy for the most representative conformation was calculated using 400 snapshots (Fig. 5C, 10–50 ns). For the CYP2E1–4*n*VPA conformations showed during the simulation, the binding free energy for the most predominant conformation was estimated using 400 snapshots (Fig. 5G, 10–50 ns). The MM-GBSA method can be conceptually summarized as:

$$\Delta G_{\text{bind}} = \Delta G_{\text{complex}} - \Delta G_{\text{receptor}}\, \Delta G_{\text{ligand}} \quad (1)$$

$$\Delta G_{\text{bind}} = \Delta H - T\,\Delta S \quad (2)$$

where $\Delta G_{\text{complex}}$, $\Delta G_{\text{receptor}}$, and ΔG_{ligand} are the free energies of complex, CYPs and VPA or 4*n*VPA, respectively. ΔH of the system is composed of the enthalpy changes in the gas phase upon complex formation (ΔE_{MM}) and the solvated free energy contribution (ΔG_{sol}), while $-T\,\Delta S$ refers to the entropy contribution to the binding. Eq. (2) can be then approximated as shown in the following equation:

$$\Delta G_{\text{bind}} = \Delta E_{\text{MM}} + \Delta G_{\text{sol}} - T\,\Delta S \quad (3)$$

$$\Delta E_{\text{MM}} + \Delta E_{\text{vdw}} + \Delta E_{\text{els}} + \Delta E_{\text{int}} \quad (4)$$

$$\Delta G_{\text{sol}} = \Delta G_{\text{els,sol}} + \Delta G_{\text{nonpolar,sol}} \quad (5)$$

where ΔE_{MM} is the summation of the van der Waals (ΔE_{vdw}), electrostatic energies (ΔE_{ele}) and torsional angle energies (ΔE_{int}).

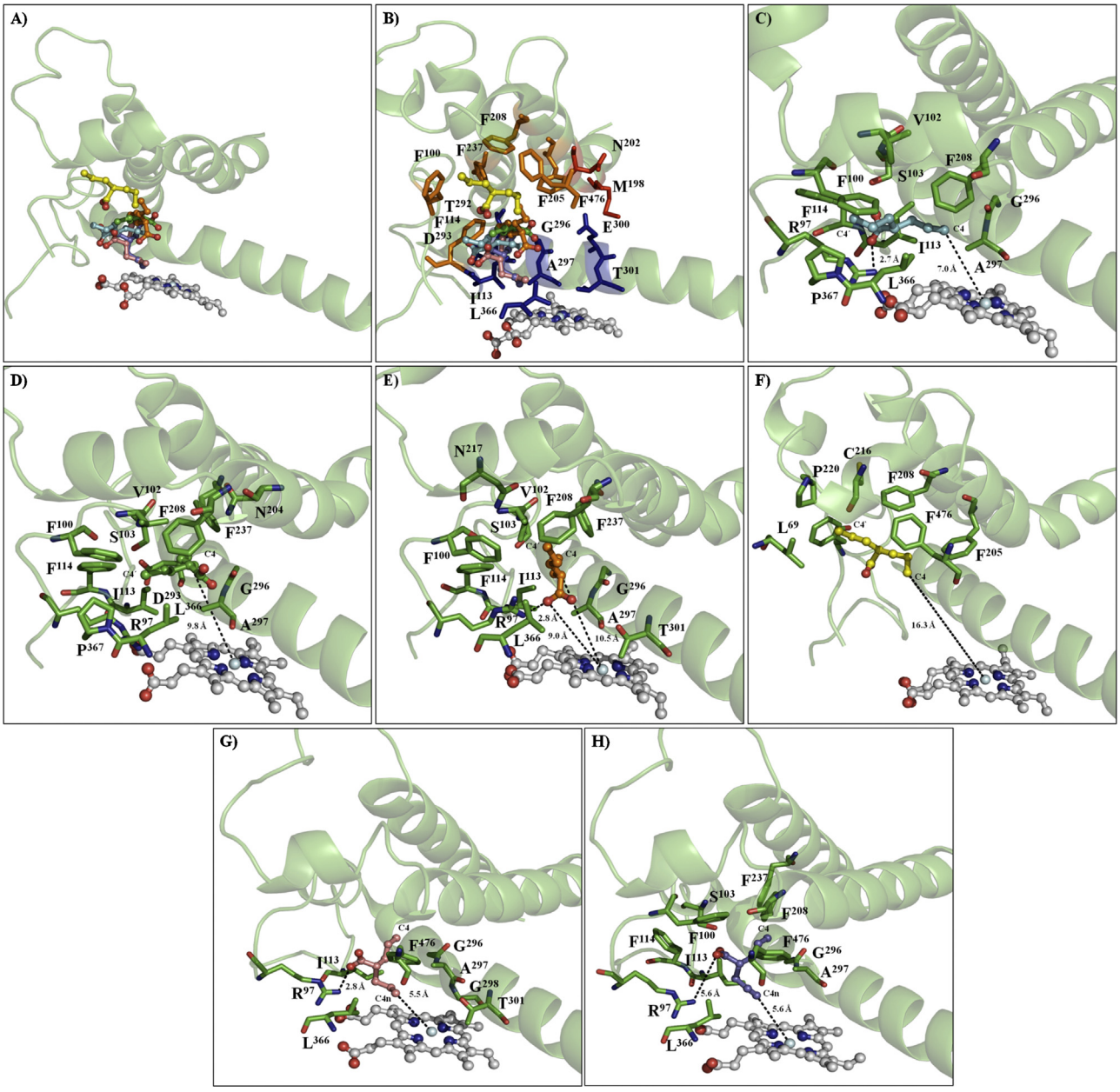

Fig. 4. Average conformations of VPA or 4*n*VPA into the active site of CYP2C11. (A) Structural superposition of the average conformations of CYP2C11–VPA, and CYP2C11–4*n*VPA complex. (B) Residues constituting the hydrophobic cleft (I^{113}, T^{292}, D^{293}, G^{296}, A^{297}, E^{300}, T^{301}, and L^{366}), narrow solvent channel (N^{202}, and M^{198}), and the Phe cluster (F^{100}, F^{114}, F^{205}, F^{208}, F^{237}, and F^{476}), are rendered as blue, orange and red stick representations, respectively. Conformation presented during the first 25-ns (C), two conformations available after 25-ns and until the 30-ns ((D) and (E)), and the conformation presented from 30 to 50 ns (F). (G) The first and the most representative CYP2C11–4*n*VPA conformation present from 10 to 45 ns, and the second conformation present during the last 5 ns (H).

In addition, ΔG_{sol} denotes the solvatation free energy that can be computed as the summation of an electrostatic component ($\Delta G_{ele,sol}$) and a non-polar component ($\Delta G_{non\text{-}polar,sol}$), and $-T\Delta S$ the contribution from the conformational entropy.

Entropic contributions were evaluated using MMPBSA.py module implemented in Amber Tools 1.5 [57], only 20 snapshots taken at time intervals of 200 ps were chosen. Because of the large memory demanding for this calculation, we did not use the entire system, therefore, an approach reported elsewhere [68], which only residues with any atom within 8 Å of the ligand in the last conformation (truncated system) were considered to perform the entropy calculation.

3. Results

3.1. Sequence alignment results

The sequence alignment among CYP2C11 sequence and those of the two templates (CYP2C9, 1R9O) and (CYP2E1, 1KOH) was carried out, and the protein sequence alignment is shown in Fig. 6. This analysis shows that the amino acid sequence of the aligned protein templates of chain A of CYP2C9 (1R9O) exhibited the highest percentage of identity with that of CYP2C11 in the range of 74.42%. The percentage of identity between the chain A of CYP2C9 (1R9O) and the chain A of CYP2E1 (1KOH) was 58.4%, whereas the percentage of identity between CYP2C11 sequence (Swiss-prot

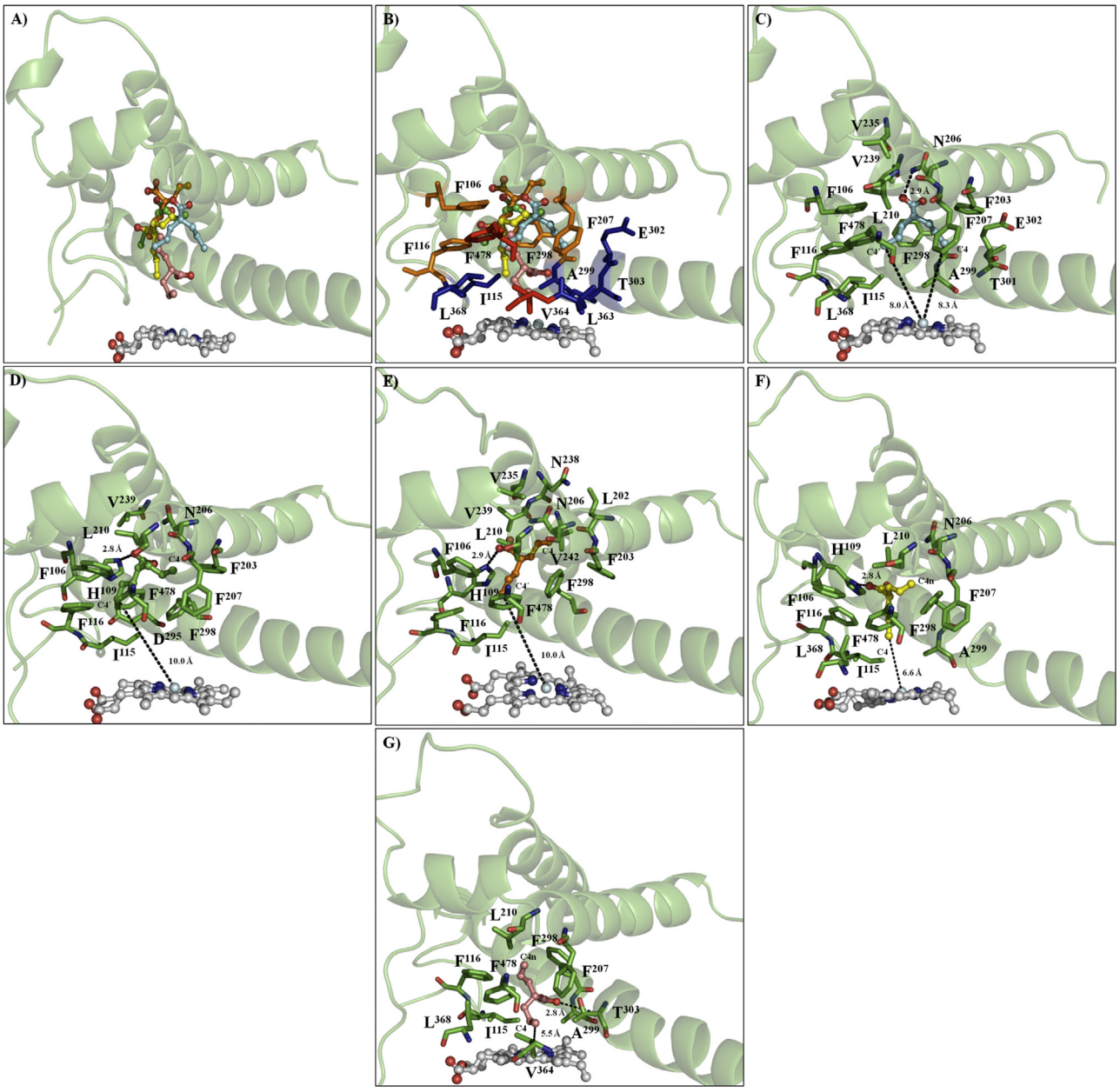

Fig. 5. Average conformations of VPA and 4*n*VPA into the active site of CYP2E1. (A) Structural superposition of the average conformations of CYP2C11–VPA, and CYP2C11–4*n*VPA complex. (B) Residues constituting the hydrophobic cleft (I^{115}, E^{302}, A^{299}, T^{303}, L^{363}, V^{364}, and L^{368}), narrow solvent channel (V^{364} and F^{478}), and the Phe cluster (F^{106}, F^{116}, F^{207}, F^{298}, and F^{478}), are rendered as blue, orange and red stick representations, respectively. Two VPA conformations presented during the first 3-ns ((C) and (D)), and the third VPA conformation presented after 3-ns and until the end of the MD simulation (E). Conformation between 4*n*VPA and CYP2E1 during the first 10-ns (F), and the most representative conformation present after this time and until the end of the MD simulation (G).

entry code: P08683), and the chain A of CYP2E1 (1KOH) was 57.6%. Furthermore, this analysis shows that several residues lining the substrate binding site are conserved or highly conserved among the three CYPs: R^{97}, I/V^{113}, F^{114}, N^{204}, S^{209}, N^{217}, N^{238}, T^{301}, D^{293}, A^{297}, E^{300}, T^{304}, L^{361}, L^{366},P^{367}, and F^{476}, that are R^{100}, I^{115}, F^{116}, N^{206}, S^{211}, N^{219}, N^{240}, T^{303}, D^{295}, A^{299}, E^{302}, T^{306}, L^{363}, L^{368}, P^{369}, and F^{478} in CYP2E1 (Fig. 6). Whereas some residues are only conserved between two CYPs: between CYP2C9 and CYP2C11 (F^{100}), CYP2C11 and CYP2E1 (F^{205}/F^{207}) or CYP2C9 and CYP2E1 (L^{208}/L^{210}). Overall, these results show that despite the low sequence identity (20%) between some CYPs [23], the three CYPs studied here possess a relative high level of sequence identity which is present not only along their overall folding structures but also at the substrate binding sites.

3.2. Docking results

It has been reported that CYP2C9 and CYP2C11 possess activity toward VPA and although 4*n*VPA only constitutes one of the multiple secondary metabolites product of VPA metabolism, is the one with hepatotoxic properties and the main product of its dehydrogenation pathway [9]. On the other hand, despite CYP2E1 shows a marginal activity toward VPA [42], it was used for exploring the ligand orientation that is responsible of the low activity of this isoform toward it. The C4 site has been pointed out [9,11] as the site that undergoes site reaction mechanism, but detailed binding orientations and interaction profiles between these enzymes and VPA or 4*n*VPA were not reported until now. Therefore, in order to evaluate the binding pose of VPA and 4*n*VPA

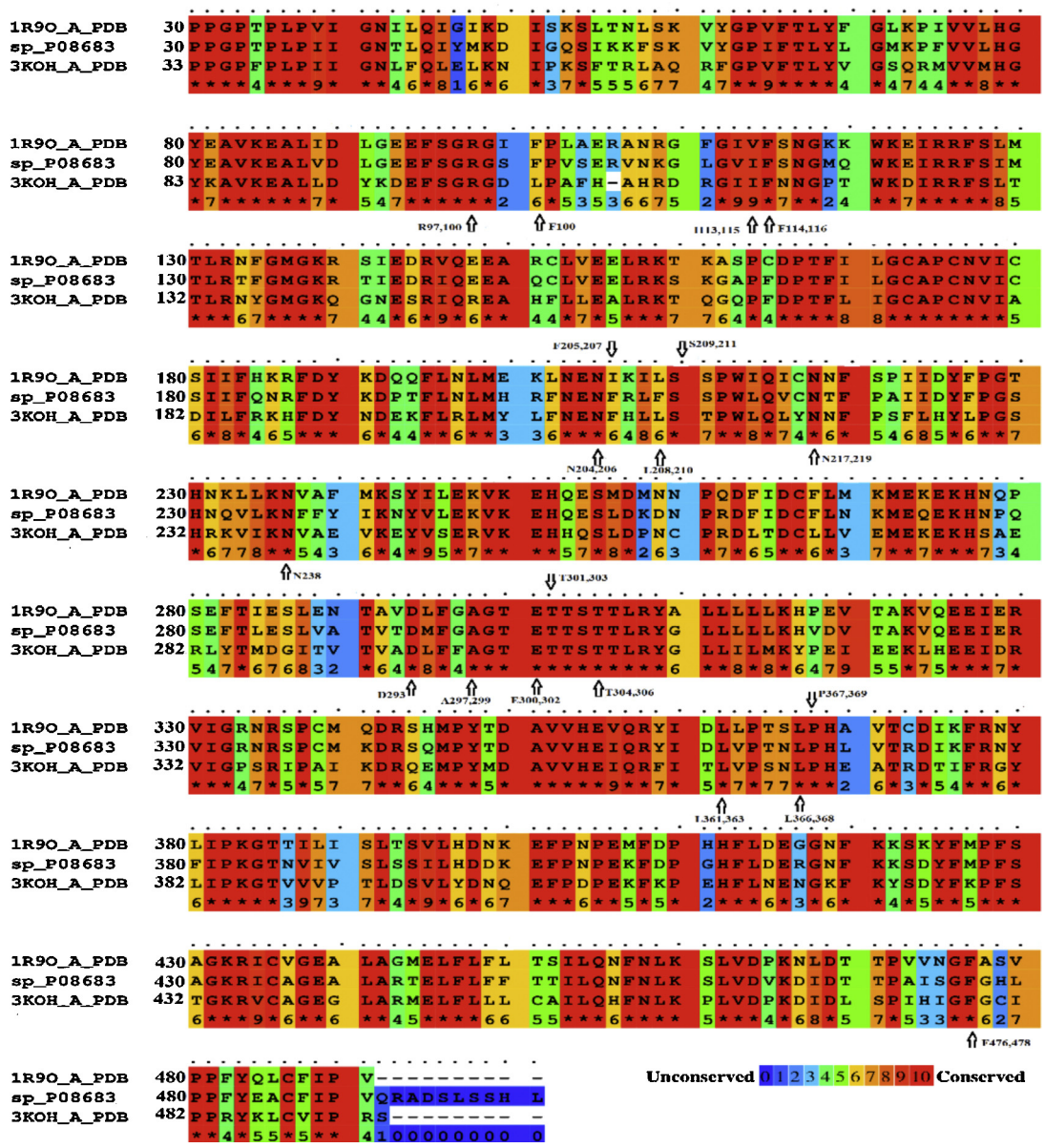

Fig. 6. The sequence alignment among chain A of flurbiprofen-bound CYP2C9 (PDB code: 1R9O), CYP2C11 (Swiss-prot entry code: P08683), and chain A of omega-imidazolyl octanoic acid-bound CYP2E1 (PDB code: 3KOH). The first 29, 29, and 32 amino acids of these proteins, respectively, are not shown, and the amino acid sequence of chain B of 3KOH was deleted due to their identical amino acid composition to chain A. Conserved or highly conserved residues lining the substrate binding site are indicated by black arrows, whereas the level of conservation is stressed by different colors. The sequence alignment was performed using PRALINE server [50].

into the binding site of CYPs, both ligands were docked into these three CYPs. From this analysis, it was observed that both ligands reached the substrate binding site which is formed by helices I, F, G, loop F–G, and loop B–C (Fig. 2B), with the hydroxyl group (R–OH) moiety oriented toward the heme and close to the iron (Fe) atom, with an average distance of less than 4.0 Å (Fig. 2C–E). Our results, demonstrated that the interactions coordinating the substrate are predominantly hydrophobic as observed in some crystallographic complexes. In Fig. 2C–E, it can be observed the residues within 4 Å involved in stabilizing the complexes where most of these residues are making hydrophobic interactions through their side chains: V^{113}, A^{297}, T^{301}, L^{362}, and L^{366} were establishing hydrophobic interactions with the ligand in the CYP2C9–VPA and CYP2C9–4*n*VPA complexes (Fig. 2C). The residues A^{297}, G^{296}, F^{205}, T^{301}, L^{361}, and V^{362} are the most involved in the CYP2C11–VPA and CYP2C11–4*n*VPA complex (Fig. 2D). Otherwise, the residues I^{115}, F^{116}, F^{207}, A^{299}, T^{303}, V^{364}, L^{368}, and F^{478} are those that interact in the CYP2E1–VPA and CYP2E1–4*n*VPA complexes (Fig. 2E). In overall, both ligands were positioned in essentially the same binding pose into the three CYPs binding sites, even when some chemical differences are present in both ligands.

Structural comparisons between the ligand orientation obtained in this study through docking procedures and that obtained using the same methodology to explore the dehydrogenation pathway of raloxifene [13], and even structural evidence of some X-ray complexes, point out that the lowest energy cluster predicted by Autodock for VPA or 4*n*VPA, produces a conformation which could be described as a metabolically inactive state. In contrast with our docking results, a metabolically active conformation was reported for the 2C9–VPA complex using a methodology that coupled the ROCS overlay method [69] and the docking program FRED [70], in which the C4 atom was oriented toward the FE atom [71]. Moreover, a MD simulation study on the picoseconds time scale reported that VPA was coupled into the substrate binding site of $P450_{cam}$ in a ligand conformation that oriented C4 toward FE atom, whereas that the carbonyl group stabilized

through electrostatic interactions [11]. On the other hand, it has been stated that the bound pose with the lowest binding energy does not correspond in most cases to the metabolically active conformation [72], and that given the diverse nature of the validation set of each docking program, it is expected that some proteins will be easier to predict than others [73]. Besides, the inclusion of flexibility and water molecules in protein binding sites also have important ramifications in docking poses of substrates in the CYP active sites [72]. Therefore, MD simulations were performed to refine the map of interactions of VPA and 4*n*VPA in the three CYPS, since that it has been reported that the fact of including flexibility to the docked conformation might reduce the risk associated with inadequate ligand conformation [74].

3.3. Molecular dynamics (MD) simulations

The robustness and stability of the predicted 3D structures of CYPs–VPA and CYPs–4*n*VPA complexes obtained using docking methods were verified through MD simulations. Interestingly, during the first ns, all ligand conformations predicted by the Autodock scoring function were lost and other conformations present, where the aliphatic section of either VPA or 4*n*VPA was oriented toward the heme group, were stabilized through hydrophobic interactions, whereas the polar moiety was stabilized by hydrogen bonds.

3.4. MD results

The robustness and stability of the predicted 3D structures of CYPs–VPA and CYPs–4*n*VPA complexes obtained using docking methods were further verified through MD simulations. Interestingly, for all the cases, at first ns the ligand conformations predicted by Autodock scoring function were lost and other conformations were present where the aliphatic section of either VPA or 4*n*VPA was oriented toward the heme group, being stabilized through hydrophobic interactions whereas the polar moiety by hydrogen bonds.

According to the 50 ns MD simulation for the structure of CYPs complexes, the RMSD for the α-carbon of CYPs as a function of the simulation time became equilibrated for the last 40 ns, with RMSD values that oscillated between 4.0 and 6.0 Å for all the complexes, values in agreement with those observed for the MD simulation studies between CYP2C9 and (S)-warfarin [75].

3.5. Interactional analysis and average properties

3.5.1. The case of CYP2C9

Structural analysis of different CYP complexes has allowed to describe the different components of the substrate binding site, which is mainly constituted by three parts: hydrophobic cleft that consist of V^{113}, L^{201}, N^{204}, I^{205}, L^{208}, V^{292}, G^{296}, A^{297}, E^{300}, and L^{366}, a ceiling which consist of the Phe cluster (F^{100}, F^{114} and F^{476}), and narrow solvent channel residues (R^{108}, and L^{102}) (Fig. 3B). For the CYP2C9–VPA complex was observed that at the first ns of MD simulations, the complex obtained through docking procedures (see Section 2.2) changed, giving place to another conformation where the polar interaction between the carboxylic moiety and the heme group was lost (Figs. 2C and 3C). In this new conformation, VPA packs next to helix I in a hydrophobic cleft that is formed by V^{113}, L^{201}, N^{204}, I^{205}, L^{208}, V^{292}, G^{296}, A^{297}, E^{301}, and L^{366}, the Phe cluster (F^{100}, F^{114} and F^{476}), and R^{108} (Fig. 3C), placing to VPA in close proximity to the second most preferred channel named pw2e [76] (Fig. 3B and C). Map of contacts that are in agreement with those observed for the crystallographic complex between 2C9 and flurbiprofen (FLP) [77] (Fig. 3B). In this latter complex, FLP is positioned with the site of hydroxylation located for oxidative attack by the reactive, hypervalent iron-oxo intermediate derived from reduction of molecular oxygen by the enzyme [77]. For VPA, the aliphatic section was stabilized by several hydrophobic residues and placing the site of dehydrogenation (C4 atom) resides 6.7 Å from the heme iron (Fig. 3C), which is consistent with the distances seen in other CYP substrate complexes [77].

For the CYP2C9–4*n*VPA complex is observed that 4*n*VPA preferred another conformation so different than that observed for VPA, where the polar moiety was hydrogen bonding to N^{474} and K^{206}, whereas the aliphatic section was stabilized by several hydrophobic contacts either backbone or side-chain atoms. This ligand conformation shared few apolar contacts observed for VPA and the site susceptible to undergo a dehydrogenation reaction was localized in a farther distance (Fig. 3D). 4*n*VPA was located between helices F and I and the turn in the C-terminal antiparallel β-sheet. Interestingly, despite this region has been seen as a narrow solvent channel (pw2c channel) formed by I^{205}, S^{209}, and E^{300} and V^{479} in the crystal structure, this is only wide enough for water molecules to enter, and catalogued as narrower than pw2e channel [78]. MD simulations allowed to observe the increase of its width, which was attributed to the backbone and side-chain movements of I^{205} and S^{209} (mobile F helix) as well as side-chain movements of E^{300} (stable I helix) because of their interactions with the ligand [75], suggesting that the narrow channel might be stabilized and widened in presence of substrate. Nevertheless, in this study we did not observe significant changes in the channel width, which slightly opened with distances between 7.5 and 9.5 Å.

3.5.2. The case of CYP2C11

Despite the lack of structural information about the CYP2C11 structure, some models have been constructed using molecular modeling techniques and also coupled with organic molecules such as testosterone [35]. From these studies, it is known that ligands are mostly coordinated in the substrate-binding site of CYP2C11, which includes a hydrophobic cleft constituted by I^{113}, T^{292}, D^{293}, G^{296}, A^{297}, E^{300}, T^{301}, and L^{366}, a ceiling which consist of the Phe cluster (F^{100}, F^{114}, F^{205}, F^{208}, F^{237}, and F^{476}) (Fig. 4B) [79]. From which, nine of these amino acid residues, namely F^{100}, F^{114}, D^{293}, G^{296}, A^{297}, E^{300}, T^{301} L^{366}, and F^{476} corresponded identically to the key amino acid residues identified in the crystallographic CYP2C9–FLP complex (1R9O), whereas that the Phe cluster at the ceiling (F^{100}, F^{114}, F^{205}, F^{208}, F^{237}, and F^{476}) is similar to that of human CYP3A4 [35]. On the other hand, as far as we are concerned, until now there is not information about its solvent channels. Therefore, in this study we evaluated the solvent channels for the different complexes of CYP2C11–VPA or CYP2C11–4*n*VPA obtained along the MD simulations using the MOLE program, which is designed for channel identification in macromolecules [80]. Derived from this latter analysis, several channels were found which exhibited a bottleneck radii smaller than 1.4 Å, which is the radius of the water molecule. However, a channel constituted by N^{202}, P^{480}, R^{307}, T^{167}, M^{198}, F^{168}, and H^{199} was found (data not shown) in most of the complexes with a radii of 1.6–2.0 Å, and with bottleneck radii of 1.46 Å, suggesting a possible pathway to the entrance/exit of ligand, forming M^{198}, and N^{202} the narrowest part of the substrate access channel (Fig. 4B).

For the CYP2C11–VPA complex were observed four ligand conformations along the 50-ns long MD simulations. At the first ns of MD simulations, the complex obtained through docking procedures (see Section 2.2) changed as observed for CYP2C9–VPA, giving place to a ligand conformation where the carboxylic moiety established hydrogen bonds with R^{97} and a polar backbone atom of F^{114}, whereas the aliphatic chain was stabilized by several members of the Phe cluster, as observed for other homology modeling complexes [35]. This ligand conformation placed the C4

atom in a distance of 7.0 Å from Fe. This first conformation was present during the half of the MD simulations time (the first 25-ns) (Fig. 4C). After this time and until the 30-ns long MD simulation, VPA was still coordinated by several members of the Phe cluster, but the ligand adopted another conformations in which VPA was basically coordinated by hydrophobic interactions (Fig. 4D and E) and the closest C4 atom (C4 or C4′) was into a atomic distance of 9.8 and 10.5 Å, whereas that the keto group was stabilized by R^{97} and looking toward the Fe atom into a distance of 9.0 Å (Fig. 4E). Then, after this time and until the end of the MD simulation, VPA was placed in another protein region close to the substrate binding site and three Phe cluster members still made contacts with VPA (Fig. 4F). Although the more representative ligand conformations suggest that this ligand position could be consistent with that required to experience a dehydrogenation reaction, the other placed the ligand in a distance that would not allow the catalysis to occur as proposed by several studies [81].

For the CYP2C11–4*n*VPA complex two conformations were present, in the first and the most representative conformation of 4*n*VPA (Fig. 4G, 10 to 45 ns), this was coordinated by a number of residues also present in the CYP2C11–VPA complex (Fig. 4C–F and G–H). In this ligand conformation, only a residue that belongs to the Phe cluster was observed (F^{476}), whereas the keto group formed a salt bridge with R^{97}, in a similar manner to that observed for CYP2C11–VPA (Fig. 4C). In contrast, the second conformation (Fig. 4H, 45 to 50 ns) was mostly stabilized by a member of the Phe cluster but by a less energetically optimized salt bridge between the keto group and R^{97}. Nevertheless, both ligand configurations placed the reduced C4 atom (C4*n*) into a similar distance from the Fe atom, shorter distance than that observed for VPA, suggesting that the reduced metabolite could be able to experience a further catalysis reaction (Fig. 4G–H).

3.5.3. The case of CYP2E1

CYP2E1 catalyzes oxidative reaction of not only low molecular weight xenobiotic compounds such as ethanol, but also endogenous fatty acids [82]. In contrast with CYP2C11 and CYP2C9 whose cavities are wide enough to accept bulky ligands, CYP2E1 is characterized by catalyzing small weight compounds and large fatty acids [82] and its active site size is considered as the smallest (~200 $Å^3$) among human CYPs [83]. The structural feature might be responsible for the advantageous of CYP2E1 over the others CYPs to metabolize small weight compounds, then creating speculation about whether the pathways in CYP2E1 will differ from those found in other mammalian CYPs [82]. In the course of multiple co-crystallized complexes, it has been elucidated that as observed for CYP2C9 and CYP2C11 complexes, several conserved residues lining a hydrophobic cleft participate in the complex stabilization: I^{115}, E^{302}, A^{299}, L^{363}, V^{364}, and, L^{368}. The Phe-cluster is also present, including to F^{106}, F^{116}, F^{207}, F^{298}, and F^{478}, which forms a ceiling on the binding pocket and blocked the channel 2c [82], as well as T^{303} which is localized in helix I and plays an important role in the substrate recognizing and positioning by establishing hydrogen bonds with the substrate in the active site [84], whereas that V^{364} and F^{478} form the narrowest part of the substrate access channel, allowing substrate or solvent entering into or release [84] (Fig. 5B). Furthermore, punctual mutations over residues such as $F^{478}V$ showed to increase 7-ethoxy-4-trifluoromethylcoumarin deethylation activity but lower *p*-nitrophenol hydroxylation activity than wild type CYP2E1, indicating that these residues are important for the specificity of this isoform [85]. Although it has been reported a minimal inhibition activity of VPA on CYP2E1, the ligand orientation of VPA was explored to gain insight about this behavior [42].

At the beginning of the simulation, the ligand conformation presented in the docked CYP2E1–VPA complex (Fig. 2E) was lost as observed for the CYP2C9–VPA and CYP2C11–VPA complexes, giving place to three energetically allowed states where the two first states were present during the three first ns and the third state started after 3 ns time and lasted almost during all the MD simulation. From Fig. 5C–E, it can be observed that VPA was mostly coordinated by residues that belong to the Phe cluster (F^{106}, F^{116}, F^{207}, F^{298}, and F^{478}), which has been reported as important in the stabilization of some complexes obtained through crystallographic procedures [81,82] and also using MD simulations [84] whereas the polar group was forming salt bridges either with N^{206} or H^{109} or simultaneously with both residues. Interestingly, T^{303} has been observed to play an important role in stabilizing and positioning the ligand through its interaction by a hydrogen bond [84]. In contrast, for the case of VPA, is observed that one of the residues that stabilize the polar group was N^{206}, which also is seen to establish a hydrogen bond with the ligand in the co-crystallized complex between CYP2E1 and the omega-imidazolyl octanoic acid [83]. Furthermore, as observed for the CYP2C9 and CYP2C11 complexes, a cluster of Phe also was involved in stabilizing the VPA molecule. However, in contrast with the favorable ligand conformations showed by CYP2C9 and CYP2C11 complexes, the three ligand conformations present here, did not produce a ligand orientation that could be able to participate in an oxide-reduction reaction, since both C4 atoms were positioned into a distance between 8.0 and 10.0 Å from Fe atom, distance slightly higher in comparison with that reported for some static complexes [84] and another gotten through MD simulations [85].

For the CYP2E1–4*n*VPA complex was found that two states were experienced by 4*n*VPA into the substrate-binding site. Fig. 5F–G shows that 4*n*VPA was coordinated by almost the same type of residues than for CYP2E1–VPA. However, 4*n*VPA adopted another position that allowed it to establish a closer contact between C4 and the Fe atom, suggesting that perhaps this enzyme possess a higher affinity for the reduced metabolite rather than the native molecule.

3.6. Calculation of the binding free energy for the CYP's-ligand complexes

To gain more information about the energetic contribution between the residues surrounding the binding site and the ligand, the electrostatic energies, non-polar solvatation, Van der Waals interactions and total contribution of the residues to the binding free energy were calculated with the molecular mechanics generalized born surface area (MM-GBSA) method [86,87] (see Section 2). This analysis shows that the complex formation is mainly driven by the non-polar ($\Delta E_{vwd} + \Delta G_{npol,sol}$) contributions, being ΔE_{vwd} interactions those that make the major contribution, whereas that the polar ($\Delta E_{ele} + \Delta G_{ele,sol}$) interactions contributed scarcely or opposed to the binding (Table 1). Thermodynamic behavior that is supported by the map of interactions observed for each of the representative VPA and 4*n*VPA binding models, where is visualized that all the complexes are mainly stabilized through hydrophobic interactions (Fig. 7). The calculated binding free energy (DG_{bind}) was more energetically favorable for the complexes formed between CYP2C9, CYP2C11 or CYP2E1 and VPA, being the highest for the CYP2C11–VPA complex (CYP2C11–VPA_c). In contrast, all the complexes between the three CYPs and 4*n*VPA produced smaller binding free energies and even unfavorable were observed for the CYP2C11–4*n*VPA complex. The entropic component was consistent among all the complexes, revealing that upon complex formation a decrement in their degrees of freedom is present which contributes with an unfavorable entropy component to the calculated binding free energy.

Table 1
Binding free energy components of CYP's-ligand complexes (in units of kcal/mol).

System	ΔE_{vdw}	ΔE_{ele}	$\Delta G_{ele,sol}$	$\Delta G_{npol,sol}$	ΔE_{polar}	ΔE_{npol}	DG_{mmgbsa}	$-T\Delta S$	DG_{bind}
CYP2C9–VPA	−17.0 (0.15)	−242.3 (1.3)	240.5 (1.2)	−2.65 (0.02)	−1.80	−19.65	−21.45 (0.2)	−16.40 (3.0)	−5.05
CYP2C9–4*n*VPA	−18.90 (0.15)	−203.0 (0.72)	206.3 (0.6)	−3.31 (0.01)	3.30	−22.21	−18.91 (0.20)	−15.36 (1.4)	−3.55
CYP2C11–VPA_c	−21.0 (0.23)	−255.0 (1.1)	256.34 (0.91)	−3.24 (0.01)	1.40	−24.24	−22.84 (0.3)	−15.91 (1.15)	−6.93
CYP2C11–VPA_{d-e}	−18.95 (0.10)	−200.0 (0.7)	206.0 (0.51)	−2.74 (0.01)	6.0	−21.69	−15.69 (0.15)	−16.64 (2.10)	+0.95
CYP2C11–VPA_f	−16.24 (0.10)	−177.4 (0.40)	187.0 (0.40)	−2.20 (0.01)	9.6	−18.44	−8.84 (0.10)	−17.11 (1.6)	+8.27
CYP2C11–4*n*VPA	−12.1 (0.7)	−153.0 (10.1)	157.0 (10.2)	−2.01 (0.10)	4.0	−14.2	−10.2 ± 0.73	−19.0 ± 4.21	+8.80
CYP2E1−VPA	−19.0 (0.3)	−351.0 (4.0)	348.0 (4.0)	−3.20 (0.04)	−3.0	−22.2	−25.0 ± 0.35	−19.60 ± 2.75	−5.40
CYP2E1−4*n*VPA	−16.6 (0.12)	−337.0 (0.66)	343.0 (0.58)	−2.77 (0.01)	6.0	−19.37	−13.37 (0.15)	−12.20 ± 5.73	−1.17

The polar ($\Delta E_{ele} + \Delta G_{ele,sol}$) contributions ($\Delta E_{polar}$) and the non-polar ($\Delta E_{vwd} + \Delta G_{npol,sol}$) contributions ($\Delta E_{npol}$). All the energies are averaged over several snapshots (see Section 2) and are in kcal/mol (±standard error of the mean).

4. Discussion

In silico methods have been widely used to investigate important features of CYPs, and particularly focused on the CYP2C9 active site [85,88,89] with the aim to predict positions of oxidation and determine important structural features that confer selectivity. Initially, because of the lack of structural information, CYPs structures were obtained through homology modeling procedures. Nowadays the availableness of several structures of CYPs has been so useful to further improve our knowledge about the ligand recognition between several organic molecules and CYPs molecules. Among these structures, CYP2C9 was one of the first structures released in the PDB forming complex with warfarin (PDB entry, 1OG5), although this complex showed an unproductive ligand conformation because the substrate lies in a mostly hydrophobic cavity at a distance of 10 Å from the heme unit [71]. MD simulation allowed to explore several ligand conformations in which warfarin was positioned in a favorable distance as to undergo a 6-7-hydroxylation [75], with a marked geometrical preference for position 7 over position 6 and also with an important structural contribution of F^{476}. Furthermore, analysis of the substrate cavity of CYP2C9 (470 $Å^3$) and NMR studies indicated that this isoform is able to bind two different ligands simultaneously [90]. Later on, other crystal structure of CYP2C9 was published with FLP bound (PDB entry, 1R9O), which is known to undergo oxidation, primarily by 4′-hydroxylation. For this complex, in contrast with that observed in the 1OG5 structure, the 4′-oxidation site was within an appropriate distance for oxidative attack by the reactive hypervalent iron-oxo intermediate derived from the reduction of molecular oxygen by CYP2C9. Substrate-heme distance that is in agreement with that observed through NMR studies was between 3.3 and 6.2 Å [91]. The lack of 3D information of several complexes between CYPs and some molecules for which experimental evidence about their hydroxylation or dehydrogenation has been observed, has led to choose some computational approaches, such as docking procedures to gain insight into the reaction mechanism [13,36]. However, this method is limited to some extend by poor contribution of the protein flexibility and some other factors [38]. Therefore, molecular docking and molecular simulation have been combined to tackle the environment problems including oxidative polymerization of alkyl phenols [92], but up to date a combined approach of these two methods to model CYPs has not been used. To address this issue, we performed molecular docking and MD simulations using available structural information (CYP2C9 and CYP2E1) and also homology modeling techniques (CYP2C11) to obtain our proteins, which then were coupled though docking procedures and simulated for 50 ns using MD simulations. Our docking results revealed that a common ligand conformation into the binding site of the three CYPs was present for both VPA and its reduced metabolite 4*n*VPA, in which the polar moiety was making interaction with the heme group into a distance of 4 Å, whereas that the potentially place to experience an electrophilic attack was in a opposed orientation to the center ferric atom of the heme group. This conformation was modified at first ns of MD simulations, leading to a range of energetically accessible ligand conformations for the three CYPs. For all the systems was observed that the aliphatic section of VPA was stabilized by hydrophobic residues, but for CYP2C11 and CYP2E1 a higher number of Phe residues was seen coordinating the VPA than for CYP2C9, whereas the polar moiety was hydrogen bonding to polar residues and for most the residues observed stabilizing these complexes there is structural evidence [35,77]. DG_{bind} values were more energetically favorable for the complexes formed between CYP2C9, CYP2C11 or CYP2E1 and VPA than for 4*n*VPA, corroborating the expected high affinity for VPA than for the reduced metabolite.

For the CYP2C9–VPA complex only one VPA conformation was present in which the closest C4 atom was positioned into an atomic distance (6.7 Å) for electrophilic attack, which is consistent with the distances seen in other CYP2C9 substrate complexes [77]. In contrast, for the CYP2C9–4*n*VPA complex, 4*n*VPA adopted another conformation so different than that observed for VPA, in which was located in close proximity to a water channel observed through MD simulations [75]. The susceptible site (C4 atom) to undergo a second dehydrogenation reaction was localized in a farther distance than for VPA. Both results are characteristic of an inactive substrate that is being expelled out of the catalytic binding site.

Four ligand states were present for VPA in the CYP2C11–VPA complex where the most predominantly VPA conformation placed the closest C4 atom into a distance of 7.0 Å from Fe atom, distance consistent with that required to experience a dehydrogenation reaction, whereas the other three remaining states would not allow the catalysis to occur as proposed by several studies [81]. For the CYP2C11–4*n*VPA complex two states were present from which the most representative 4*n*VPA conformation placed the reduced C4 atom (C4*n*) into a similar distance from the Fe atom, in a shorter distance than that observed for VPA, suggesting that the reduced metabolite could be able to experience a further catalysis reaction.

For the CYP2E1–VPA complex three energetically states were present where the most representative state did not produce a ligand orientation that could be able to participate in an oxide-reduction reaction, since both C4 atoms were positioned into a distance between 8 and 10.0 Å from Fe atom, distance slightly higher in comparison with that reported for some static complexes [81] and another observed through MD simulations [82]. Therefore, this less favored ligand conformation could be responsible for the minimal inhibition activity experimentally reported for this human CYP isoform [42]. For the 2E1-4*n*VPA complex, two 4*n*VPA states were present into the substrate-binding site adopted a ligand position that would allow it to establish a closer contact between C4 and the Fe atom, suggesting that perhaps this enzyme possess a higher affinity for the reduced metabolite rather than the native molecule.

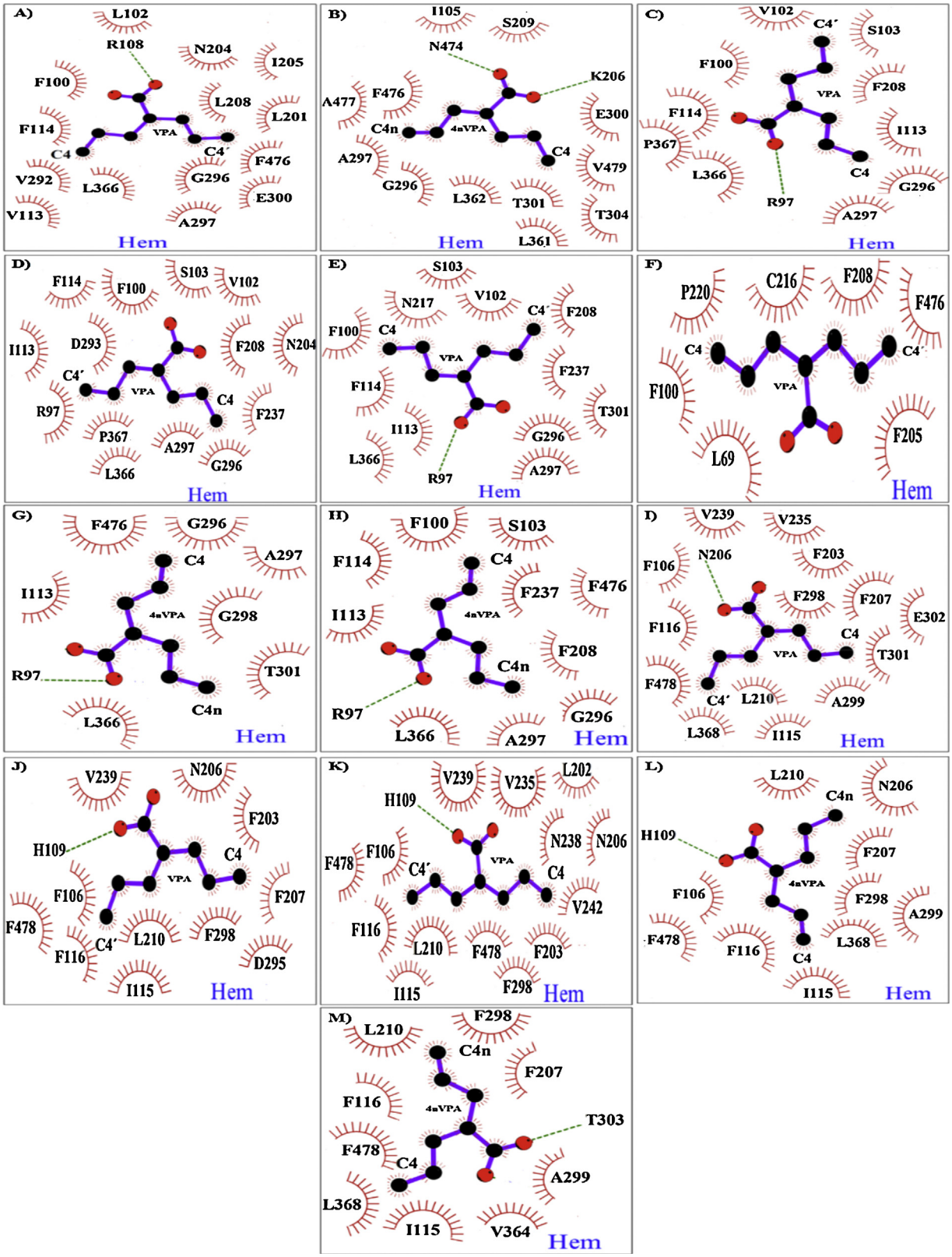

Fig. 7. Schematic representations of hydrogen bonds (green dashed lines) and hydrophobic contacts (red arc with spokes) of CYP2C9–VPA (2SA), CYP2C9–4*n*VPA (2SB), CYP2C11–VPA (2SC-F), CYP2C11–4*n*VPA (2SG and H), CYP2E1–VPA (2SI-K), and CYP2E1–4*n*VPA (2SL and M) complexes. Drawings were generated using LIGPLOT v.4.5.3 [94], and the average conformations from Figs. 3C and D, 4C–H, and 5C–G.

The multiple ligand conformations present for CYP2C11 and CYP2E1 suggest a high flexibility into the catalytic binding site that could work as an adaptative mechanism to place the substrate through subtle conformational changes that contribute to get more favorable energetic states. Furthermore, the presence of multiple binding orientations may give place for the production of multiple oxidized metabolites as observed for the case of hydroxylation of progesterone into the catalytic binding site of CYP2C5 [93].

Based on these results, it is clear that geometrical preference is regulated by the chemical nature of the substrate, the substrate binding cavity and the flexibility of the residues constituting the catalytic binding site. Therefore, the regioselectivity is a result of the chemical and shape of the protein and ligand rather than caused by local interaction near the heme oxygen as mentioned by Seifer et al. [75]. Furthermore, our results have important contribution to the details of enzyme-catalyzed reactions in the process of VPA dehydrogenation, which can broaden our knowledge of this reaction mechanism. However, in contrast to soluble bacterial CYPs, mammalian CYPs are membrane-anchor proteins bound to a lipid membrane through the N-terminal transmembrane helix, so the ligand conformation observed here may be improved in a more physiological system.

In conclusion, docking and MD simulation studies were performed to gain insight into the regioselectivity of VPA into three CYPs for which it is known to exhibit affinity. Our results showed VPA states into the CYP catalytic cavity of CYP2C9 and CYP2C11 where C4 was oriented toward the Fe atom for electrophilic attack and therefore experiences a dehydrogenation reaction, but a less favored C4 position was observed for CYP2E1, corroborating the lower affinity reported from this CYP to VPA. On the other hand, 4*n*VPA showed some differences with respect to its placing into the three CYPs. For the CYP2C9–4*n*VPA complex, 4*n*VPA not only showed a less optimized map of interactions, result that was in agreement with its unfavorable DG_{bind} value, but also was collocated close to a water channel, suggesting that 4*n*VPA is not candidate to experience further catalytic reaction in this CYP and that maybe is being expelled from the catalytic binding site. In contrast, for the CYP2C11–4*n*VPA and CYP2E1–4*n*VPA complexes, 4*n*VPA showed states that suggest further catalytic reactions because of its shorter distance to the Fe atom in comparison with the observed for VPA. However, binding free energy analysis showed unfavorable and marginal favorable DG_{bind} values for CYP2C11–4*n*VPA and CYP2E1–4*n*VPA complexes, suggesting that these states could correspond to energetic transient states. Overall, these results show that not only the chemical nature of the CYPs cavity and its intrinsic flexibility play an important role in ligand stabilizing and positioning, but also the chemical structure may have critical structural effect on the binding pose of the ligand, promoting ligand orientation toward heme group in the three CYPs.

Authors contributions

MB: project design, achieve the theoretical studies, results analyses and write the article; JMW: results analyses and write the article; JCB: project designs, results analyses and write the article.

Acknowledgments

The authors thank to Consejo Nacional de Ciencia y Tecnología (CONACYT-132353), CYTED: 214RT0482, Instituto de Ciencia y Tecnología del Distrito Federal (ICyTDF-45/2012; PIRIVE09-9) and Secretaría de Investigación y Posgrado/Comisión de Operación y Fomento de Actividades Académicas del Instituto Politécnico Nacional (SIP/COFAA-IPN-20130379; 20140252) for financial support. Martiniano Bello thanks CONACyT for a scholarship.

References

[1] Johannessen CU, Johannessen SI. Valproate: past, present and future. CNS Drug Rev 2003;9(2):199–216.
[2] Tang W, Lu AY. Metabolic bioactivation and drug-related adverse effects: current status and future directions from a pharmaceutical research perspective. Drug Metab Rev 2010;42(2):225–49.
[3] Tang W. Drug metabolite profiling and elucidation of drug-induced hepatotoxicity. Expert Opin Drug Metab Toxicol 2007;3(3):407–20.
[4] Porubek DJ, Grillo MP, Baillie TA. The covalent binding to protein of valproic acid and its hepatotoxic metabolite, 2-*n*-propyl-4-pentenoic acid, in rats and in isolated rat hepatocytes. Drug Metab Dispos 1989;17(2):123–30.
[5] Leone AM, Kao LM, McMillian MK, Nie AY, Parker JB, Kelley MF, et al. Evaluation of felbamate and other antiepileptic drug toxicity potential based on hepatic protein covalent binding and gene expression. Chem Res Toxicol 2007;20(4):600–8.
[6] Nakayama S, Atsumi R, Takakusa H, Kobayashi Y, Kurihara A, Nagai Y, et al. A zone classification system for risk assessment of idiosyncratic drug toxicity using daily dose and covalent binding. Drug Metab Dispos 2009;37(9):1970–7.
[7] Chang TK, Abbott FS. Oxidative stress as a mechanism of valproic acid-associated hepatotoxicity. Drug Metab Rev 2006;38(4):627–39.
[8] Silva MF, Aires CC, Luis PB, Ruiter JP, Ijlst L, Duran M, et al. Tavares de Almeida I valproic acid metabolism and its effects on mitochondrial fatty acid oxidation: a review. J Inherit Metab Dis 2008;31(2):205–16.
[9] Rettie AE, Boberg M, Rettenmeier AW, Baillie TA. Cytochrome P-450-catalyzed desaturation of valproic acid in vitro: species differences, induction effects, and mechanistic studies. J Biol Chem 1988;263(27):13733–38.
[10] Ortiz de Montellano PR. In: Ortiz de Montellano PR, editor. 2nd ed., Cytochrome P450: structure mechanism and biochemistry, New York, NY: Plenum Press; 1995.
[11] Collins Jack R, Camper Debra L, Loew Gilda H. Valproic acid metabolism by cytochrome P450: a theoretical study of stereoelectronic modulators of product distribution. J Am Chem Soc 1991;113:2736–43.
[12] Obach RS. Mechanism of cytochrome P4503A4- and 2D6-catalyzed dehydrogenation of ezlopitant as probed with isotope effects using five deuterated analogs. Drug Metab Dispos 2001;29(12):1599–607.
[13] Moore CD, Shahrokh K, Sontum SF, Cheatham TE, Yost GS. Improved cytochrome P450 3A4 molecular models accurately predict the Phe215 requirement for raloxifene dehydrogenation selectivity. Biochemistry 2010;49(41):9011–9.
[14] Nagata K, Liberato DJ, Gillette JR, Sasame HA. An unusual metabolite of testosterone 17 beta-hydroxy-4,6-androstadien-3-one. Drug Metab Dispos 1986;14(5):559–65.
[15] Guan X, Fisher MB, Lang DH, Zheng YM, Koop DR, Rettie AE. Cytochrome P450-dependent desaturation of lauric acid: isoform selectivity and mechanism of formation of 11-dodecenoic acid. Chem Biol Interact 1998;110(1–2):103–21.
[16] Pennanen S, Kojo A, Pasanen M, Liesivuori J, Juvonen RO, Komulainen H. CYP enzymes catalyze the formation of a terminal olefin from 2-ethylhexanoic acid in rat and human liver. Hum Exp Toxicol 1996;15(5):435–42.
[17] Ortiz de Montellano PR. In: Ortiz de Montellano PR, editor. 1st ed., Cytochrome P450: structure mechanism and miochemistry, New York, NY: Plenum Press; 1986.
[18] Dawson JH, Sono M. Cytochrome P450 and chloroperoxidase: thiolate-ligated heme enzymes spectroscopic determination of their active-site structures and mechanistic implications of thiolate ligation. Chem Rev 1987;87(5):1255–76.
[19] Sono M, Roach MP, Coulter ED, Dawson JH. Heme-containing oxygenases. Chem Rev 1996;96(7):2841–88.
[20] Woggon WD. Cytochrome P450: significance, reaction mechanisms and active site analogues. Bioorg Chem: Top Curr Chem 1997;184:39–96.
[21] Ortiz de Montellano PR, De Voss JJ. Oxidizing species in the mechanism of cytochrome P450. Nat Prod Rep 2002;19(4):477–93.
[22] Watanabe Y. Alternatives to the oxoferryl porphyrin cation radical as the proposed reactive intermediate of cytochrome P450: two-electron oxidized Fe(III) porphyrin derivatives. J Biol Inorg Chem 2001;6(8):846–56.
[23] Denisov IG, Makris TM, Sligar SG, Schlichting I. Structure and chemistry of cytochrome P450. Chem Rev 2005;105(6):2253–77.
[24] Meunier B, de Visser SP, Shaik S. Mechanism of oxidation reactions catalyzed by cytochrome p450 enzymes. Chem Rev 2004;104(9):3947–80.
[25] Kumar D, De Visser SP, Shaik S. Oxygen economy of cytochrome P450: what is the origin of the mixed functionality as a dehydrogenase–oxidase enzyme compared with its normal function? J Am Chem Soc 2004;126(16):5072–3.
[26] Kartha JS, Skordos KW, Sun H, Hall C, Easterwood LM, Reilly CA, et al. Single mutations change CYP2F3 from a dehydrogenase of 3-methylindole to an oxygenase. Biochemistry 2008;47(37):9756–70.
[27] Wen X, Wang JS, Kivistö KT, Neuvonen PJ, Backman JT. In vitro evaluation of valproic acid as an inhibitor of human cytochrome P450 isoforms: preferential inhibition of cytochrome P450 2C9 (CYP2C9). Br J Clin Pharmacol 2001;52(5):547–53.
[28] Schoch GA, Attias R, Le Ret M, Werck-Reichhart D. Key substrate recognition residues in the active site of a plant cytochrome P450, CYP73A1. Homology guided site-directed mutagenesis. Eur J Biochem 2003;270(18):3684–95.
[29] Szklarz GD, Halpert JR. Use of homology modeling in conjunction with site-directed mutagenesis for analysis of structure–function relationships of mammalian cytochromes P450. Life Sci 1997;61(26):2507–20.
[30] Lewis DF, Lake BG, Dickins M, Goldfarb PS. Homology modelling of CYP2A6 based on the CYP2C5 crystallographic template: enzyme-substrate interactions and QSARs for binding affinity and inhibition. Toxicol In Vitro 2003;17(2):179–90.
[31] Lewis DF, Lake BG, Dickins M, Goldfarb PS. Homology modelling of CYP3A4 from the CYP2C5 crystallographic template: analysis of typical CYP3A4 substrate interactions. Xenobiotica 2004;34(6):549–69.

[32] Sun H, Moore C, Dansette PM, Kumar S, Halpert JR, Yost GS. Dehydrogenation of the indoline-containing drug 4-chloro-*N*-(2-methyl-1-indolinyl)-3-sulfamoylbenzamide (indapamide) by CYP3A4: correlation with in silico predictions. Drug Metab Dispos 2009;37(3):672–84.

[33] McGovern SL, Shoichet BK. Information decay in molecular docking screens against holo, apo, and modeled conformations of enzymes. J Med Chem 2003;46(14):2895–907.

[34] Kitchen DB, Decornez H, Furr JR, Bajorath J. Docking and scoring in virtual screening for drug discovery: methods and applications. Nat Rev Drug Discovery 2004;3(11):935–49.

[35] Wang H, Cheng JD, Montgomery D, Cheng KC. Evaluation of the binding orientations of testosterone in the active site of homology models for CYP2C11 and CYP2C13. Biochem Pharmacol 2009;78(4):406–13.

[36] Cassidy CE, Setzer WN. Cancer-relevant biochemical targets of cytotoxic *Lonchocarpus* flavonoids: a molecular docking analysis. J Mol Model 2010;16(2):311–26.

[37] Wu B, Ford T, Gu JD, Zhang XX, Li AM, Cheng SP. Computational studies of interactions between endocrine disrupting chemicals and androgen receptor of different vertebrate species. Chemosphere 2010;80(5):535–41.

[38] Bello M, Martínez-Archundia M, Correa-Basurto J. Automated docking for novel drug discovery. Expert Opin Drug Discovery 2013;8(7):821–34.

[39] Dong BL, Liao QH, Wei J. Docking and molecular dynamics study on the inhibitory activity of *N,N*-disubstituted-trifluoro-3-amino-2-propanols-based inhibitors of cholesteryl ester transfer protein. J Mol Model 2011;17(7):1727–34.

[40] Anuradha CM, Mulakayala C, Babajan B, Naveen M, Rajasekhar C, Kumar CS. Probing ligand binding modes of *Mycobacterium tuberculosis* MurC ligase by molecular modeling, dynamics simulation and docking. J Mol Model 2010;16(1):77–85.

[41] Pourahmad J, Eskandari MR, Kaghazi A, Shaki F, Shahraki J, Fard JK. A new approach on valproic acid induced hepatotoxicity: involvement of lysosomal membrane leakiness and cellular proteolysis. Toxicol In Vitro 2012;26(4):545–51.

[42] Neuman MG, Shear NH, Jacobson-Brown PM, Katz GG, Neilson HK, Malkiewicz IM, et al. CYP2E1-mediated modulation of valproic acid-induced hepatocytotoxicity. Clin Biochem 2001;34(3):211–8.

[43] Sadeque AJ, Fisher MB, Korzekwa KR, Gonzalez FJ, Rettie AE. Human CYP2C9 and CYP2A6 mediate formation of the hepatotoxin 4-ene-valproic acid. J Pharmacol Exp Ther 1997;283(2):698–703.

[44] Szklarz GD, Ornstein RL, Halpert JR. Application of 3-dimensional homology modeling of cytochrome P450 2B1 for interpretation of site-directed mutagenesis results. J Biomol Struct Dyn 1994;12(1):61–78.

[45] Dannan GA, Guengerich FP, Waxman DJ. Hormonal regulation of rat liver microsomal enzymes role of gonadal steroids in programming, maintenance, and suppression of delta 4-steroid 5 alpha-reductase, flavin-containing monooxygenase, and sex-specific cytochromes P-450. J Biol Chem 1986;261(23):10728–35.

[46] Imaoka S, Fujita S, Funae Y. Age-dependent expression of cytochrome P-450s in rat liver. Biochim Biophys Acta 1991;1097(3):187–92.

[47] Danilczuk Z, Klenk-Majewska B, Ossowska G, Wielosz M. Influence of stress and dexamethasone on plasma levels of antiepileptic drugs and theophylline in rats. Ann Univ Mariae Curie Sklodowska 2010;13(1):109–16.

[48] Larkin MA, Blackshields G, Brown NP, Chenna R, McGettigan PA, McWilliam H, et al. Clustal W and Clustal X version 2.0. Bioinformatics 2007;23(21):2947–8.

[49] Zhang Y. I-TASSER server for protein 3D structure prediction. BMC Bioinf 2008;9:40.

[50] Simossis VA, Heringa J. PRALINE: a multiple sequence alignment toolbox that integrates homology-extended and secondary structure information. Nucleic Acids Res 2005;1(33):W289–94 (accessed April 15, 2013).

[51] Morris GM, Goodsell DS, Halliday RS, Huey R, Hart WE, Belew RK, et al. Automated docking using Lamarckian genetic algorithm and an empirical binding free energy function. J Comput Chem 1998;19(14):1639–62.

[52] ISIS/Draw, MDL Information System, 14600 Catalina Street, San Leandro, CA 94677, USA. The program (editions of 2.5 and 2.3) is available at the MDL at http://www.mdli.com/downloads/isisdraw.html (Accessed January 10, 2013).

[53] WebLab Viewer, available at http://www.liv.ac.uk/ctichem/16weblab.html (Accessed January 20, 2013).

[54] Flükiger PF. Development of the molecular graphics package MOLEKEL and its application to selected problems in organic and organometallic chemistry. In: Thèse no. 2561. Genève: Département de Chimie Physique, Université de Genève; 1992.

[55] HyperChem (TM) Professional 6.0. Gainesville, FL, USA: Hypercube Inc.; 1985.

[56] Frisch MJ, Trucks GW, Schlegel HB, Scuseria GE, Robb MA, Cheeseman JR, et al. Gaussian 03, revision A.1. Pittsburgh, PA: Gaussian Inc.; 2003.

[57] Case DA, Darden TA, Cheatham III TE, Simmerling CL, Wang J, Duke RE, et al. AMBER 12. San Francisco, CA: University of California; 2012.

[58] Wang J, Cieplak P, Kollman PA. How well does a restrained electrostatic potential (RESP) model perform in calculating conformational energies of organic and biological molecules? J Comput Chem 2000;21(12):1049–74.

[59] Wang J, Wolf RM, Caldwell JW, Kollman PA, Case DA. Development and testing of a general Amber force field. J Comput Chem 2004;25(9):1157–74.

[60] Jakalian A, Jack DB, Bayly CI. Fast, efficient generation of high-quality atomic charges AM1-BCC model: II. Parameterization and validation. J Comput Chem 2002;23:1623–41.

[61] Amber Parameter Database: http://www.pharmacy.manchester.ac.uk/bryce/amber (Accessed March 13, 2013).

[62] Jorgensen WL, Chandrasekhar J, Madura JD, Impey RW, Klein ML. Comparison of simple potential functions for simulating liquid water. J Chem Phys 1983;79(2):926–35.

[63] Darden T, York D, Pedersen L. Particle mesh Ewald: an *N*-log(*N*) method for Ewald sums in large systems. J Chem Phys 1993;98(12):10089–92.

[64] Van Gunsteren WF, Berendsen HJC. Algorithm for macromolecular dynamics and constraint dynamics. Mol Phys 1977;34(5):1311–27.

[65] Berendsen HJC, Postma JPM, van Gunsteren WF, DiNola A, Haak JR. Molecular dynamics with coupling to an external bath. J Chem Phys 1984;81(8):3684–90.

[66] DeLano WL. The PyMOL molecular graphics system. San Carlos, CA: DeLano Scientific; 2002, http://www.pymol.org.

[67] Hawkins GD, Cramer CJ, Truhlar DG. Parameterized models of aqueous free energies of solvation based on pairwise descreening of solute atomic charges from a dielectric medium. J Phys Chem 1996;100:19824–39.

[68] Kuhn B, Kollman PA. Binding of a diverse set of ligands to avidin and streptavidin: an accurate quantitative prediction of their relative affinities by a combination of molecular mechanics and continuum solvent models. J Med Chem 2000;43:3786–91.

[69] ROCS, Version 2.2. Santa Fe, NM: Openeye Scientific Software; 1997, http://www.eyesopen.com.

[70] FRED. Version 2.1.2: Openeye Scientific Software. Santa Fe, NM: FRED; 2005.

[71] Sykes MJ, McKinnon RA, Miners JO. Prediction of metabolism by cytochrome P450 2C9: alignment and docking studies of a validated database of substrates. J Med Chem 2008;51(4):780–91.

[72] Huang TW, Zaretzki J, Bergeron C, Bennett KP, Breneman CM. DR-predictor: incorporating flexible docking with specialized electronic reactivity and machine learning techniques to predict CYP-mediated sites of metabolism. J Chem Inf Model 2013;53(12):3352–66.

[73] Kirton SB, Murray CW, Verdonk ML, Taylor RD. Prediction of binding modes for ligands in the cytochromes P450 and other heme-containing proteins. Proteins 2005;58(4):836–44.

[74] Alonso H, Bliznyuk AA, Gready JE. Combining docking and molecular dynamic simulations in drug design. Med Res Rev 2006;26(5):531–68.

[75] Seifert A, Tatzel S, Schmid RD, Pleiss J. Multiple molecular dynamics simulations of human p450 monooxygenase CYP2C9: the molecular basis of substrate binding and regioselectivity toward warfarin. Proteins 2006;64(1):147–55.

[76] Cojocaru V, Winn PJ, Wade RC. The ins and outs of cytochrome P450s. Biochim Biophys Acta 2007;1770:390–401.

[77] Wester MR, Yano JK, Schoch GA, Yang C, Griffin KJ, Stout CD, et al. The structure of human cytochrome P450 2C9 complexed with flurbiprofen at 2.0—a resolution. J Biol Chem 2004;279(34):35630–37.

[78] Skopalík 1 J, Anzenbacher P, Otyepka M. Flexibility of human cytochromes P450: molecular dynamics reveals differences between CYPs 3A4, 2C9, and 2A6, which correlate with their substrate preferences. J Phys Chem B 2008;112(27):8165–73.

[79] Hamed IA, Yamada M, Fujita H, Akaho E. Studies on 16α-hydroxylation of steroid molecules and regioselective binding mode in homology-modeled cytochrome P450-2C11. Intern J Med Chem 2011;918168:1–11.

[80] Petrek M, Kosinova P, Koca J, Otyepka MMOLE. A Voronoi diagram based explorer of molecular channels, pores, and tunnels. Structure 2007;15:1357–63.

[81] Jovanovic T, Farid R, Friesner RA, McDermott AE. Thermal equilibrium of high- and low-spin forms of cytochrome P450 BM-3: repositioning of the substrate? J Am Chem Soc 2005;127(39):13548–52.

[82] Shen Z, Cheng F, Xu Y, Fu J, Xiao W, Shen J, et al. Investigation of indazole unbinding pathways in CYP2E1 by molecular dynamics simulations. PLoS One 2012;7(3):1–7.

[83] Porubsky PR, Meneely KM, Scott EE. Structures of human cytochrome P-450 2E1 Insights into the binding of inhibitors and both small molecular weight and fatty acid substrates. J Biol Chem 2008;283(48):33698–707.

[84] Liu Y, Liu BY, Hao P, Li X, Li YX, Wang JF. π–π stacking mediated drug-drug interactions in human CYP2E1. Proteins 2013;81(6):945–54.

[85] Afzelius L, Zamora I, Ridderström M, Andersson TB, Karlén A, Masimirembwa CM. Competitive CYP2C9 inhibitors: enzyme inhibition studies, protein homology modeling, and three-dimensional quantitative structure-activity relationship analysis. Mol Pharmacol 2001;59(4):909–19.

[86] Punkvang A, Saparpakorn P, Hannongbua S, Wolschann P, Beyer A, Pungpo P. Investigating the structural basis of arylamides to improve potency against *M. tuberculosis* strain through molecular dynamics simulations. Eur J Med Chem 2010;45(12):5585–93.

[87] Schaffner-Barbero C, Gil-Redondo R, Ruiz-Avila LB, Huecas S, Läppchen T, den Blaauwen T, et al. Insights into nucleotide recognition by cell division protein FtsZ from a mant-GTP competition assay and molecular dynamics. Biochemistry 2010;49(49):10458–72.

[88] De Groot MJ, Ekins S. Pharmacophore modeling of cytochromes P450. Adv Drug Delivery Rev 2002;54(3):367–83.

[89] De Groot MJ. Designing better drugs: predicting cytochrome P450 metabolism. Drug Discovery Today 2006;11(13–14):601–6.

[90] Melet A, Assrir N, Jean P, Lopez-Garcia PM, Marques-Soares C, Jaouen M, et al. Substrate selectivity of human cytochrome P450 2C9: importance of residues 476, 365, and 114 in recognition of diclofenac and sulfaphenazole and in

mechanism-based inactivation by tienilic acid. Arch Biochem Biophys 2003;409(1):80–91.
[91] Prasad JC, Goldstone JV, Camacho CJ, Vajda S, Stegeman JJ. Ensemble modeling of substrate binding to cytochromes P450: analysis of catalytic differences between CYP1A orthologs. Biochemistry 2007;46(10):2640–54.
[92] Park JC, Joo JC, An ES, Song BK, Kim YH, Yoo YJ. A combined approach of experiments and computational docking simulation to the *Coprinus cinereus* peroxidase-catalyzed oxidative polymerization of alkyl phenols. Bioresour Technol 2011;102(7):4901–4.
[93] Williams PA, Cosme J, Sridhar V, Johnson EF, McRee DE. Mammalian microsomal cytochrome P450 monooxygenase: structural adaptations for membrane binding and functional diversity. Mol Cell 2000;5(1):121–31.
[94] Wallace AC, Laskowski RA, Thornton JM. LIGPLOT: a program to generate schematic diagrams of protein-ligand interactions. Protein Eng 1995;8:127–34.